The Astrophysical Journal, 826:137 (6pp), 2016 August 1 doi:10.3847/0004-637X/826/2/137

DUST LOSS FROM ACTIVATED ASTEROID P/2015 X6

F. Moreno[1], J. Licandro[2,3], A. Cabrera-Lavers[1,3,4], and F. J. Pozuelos[1]
[1] Instituto de Astrofísica de Andalucía, CSIC, Glorieta de la Astronomía s/n, E-18008 Granada, Spain; fernando@iaa.es
[2] Instituto de Astrofísica de Canarias, c/Vía Láctea s/n, E-38200 La Laguna, Tenerife, Spain
[3] Departamento de Astrofísica, Universidad de La Laguna (ULL), E-38205 La Laguna, Tenerife, Spain
[4] GTC Project, E-38205 La Laguna, Tenerife, Spain
Received 2016 April 19; revised 2016 May 4; accepted 2016 May 15; published 2016 July 27

ABSTRACT

We present observations and dust tail models of activated asteroid P/2015 X6 from deep imaging data acquired at the 10.4 m Gran Telescopio Canarias (GTC) from 2015 mid-December to 2016 late January. The results of the modeling indicate that the asteroid has undergone sustained dust loss over a period of two months or longer. The dust parameters, derived from multidimensional fits of the available images, are compatible with either ice sublimation or rotational instability processes. An impulsive event, as might be associated with an impact with another body, is less likely. A power-law distribution of particles, with minimum and maximum radii of 1 μm and 1 cm and a power index of -3.3, is found to be consistent with the observations. Depending on the model of ejection velocity adopted, the particle velocities are found to be in the range of 0.3–10 m s^{-1}. The activation time was between 18 and 26 days before discovery. The total mass ejected from that time to the most recent observation is in the range 5–9 $\times$ 10^6 kg. No dust features giving indication of past activity earlier than the activation time have been observed.

Key words: methods: numerical – minor planets, asteroids: individual (P/2015 X6)

1. INTRODUCTION

The activated asteroid P/2015 X6 was discovered by Lilly & Weryk (2015) from Pan-STARRS 1 images on 2015 December 7.27. Follow-up images were obtained from several observatories until 2015 December 15, by Tubbiolo et al. (2015) from LPL/Spacewatch II. The object was described as having a nonstellar coma with a narrow tail of 6″ size toward a position angle (PA) of 75°. The available astrometry indicates that the object is asteroidal from the dynamical point of view, as its Tisserand invariant with respect to Jupiter (Kresak 1982) is $T_J = 3.32$, derived from its orbital elements $a = 2.756$ AU, $e = 0.170$, and $i = 4\overset{\circ}{.}56$. To date, more than 15 objects of this kind have been discovered. Their activity might have been triggered by a variety of processes, such as rotational instability (e.g., P/2012 F5 or P/2013 R3, Jewitt et al. 2014; Drahus et al. 2015), an impact with another object (e.g., (596) Scheila, Moreno et al. 2011b), or ice sublimation (e.g., 133P or 324P, Hsieh et al. 2010; Moreno et al. 2011a; Hsieh & Sheppard 2015), although in these latter cases no gas emission lines have been detected so far. For an in-depth review of the activation mechanisms involved and a detailed description of the individual objects, we refer to Jewitt et al. (2015). From the dynamical point of view, most of those activated asteroids are stable on timescales of 100 Myr or longer (Hsieh et al. 2012, 2013), so they are native members of the main belt, although there are two objects (238P and 259P) that are unstable on scales of only 10–20 Myr (Haghighipour 2009; Jewitt et al. 2015).

In this paper we report observations acquired with the 10.4 m GTC, and models of the brightness of the dust tail of P/2015 X6, in order to characterize its dust emission pattern, the activation time and duration of the activity, and the total dust mass lost, and we attempt to identify which mechanism(s) could be playing a role in its activation.

2. OBSERVATIONS AND DATA REDUCTION

Images of P/2015 X6 were acquired under photometric conditions on the nights of 2015 December 17 and 30, and 2016 January 7 and 25. The images were obtained using a Sloan r' filter in the Optical System for Image and Low Resolution Integrated Spectroscopy (OSIRIS) camera-spectrograph (Cepa et al. 2000; Cepa 2010, p. 15) at the GTC. OSIRIS is equipped with two Marconi CCD detectors, each with 2048 $\times$ 4096 pixels, providing a field of view of $7\overset{'}{.}8 \times 7\overset{'}{.}8$. In order to improve the signal-to-noise ratio we used 2 $\times$ 2 binning, so that the plate scale was $0\overset{''}{.}254$ px^{-1}. The seeing (FWHM) in the images ranged from $0\overset{''}{.}9$ to $1\overset{''}{.}2$. After bias subtraction and flat-field correction a median stack of the available frames was computed. The resulting images were calibrated using standard stars, and then converted to solar disk intensity units, which are the output of the dust tail code. The journal of the observations is given in Table 1, where we indicate the date of the observations (in UT and days to the asteroid's perihelion), the heliocentric (R) and geocentric (Δ) distances, the phase angle (α), the position angle of the radius vector from the Sun to the comet (PsAng), and the angle between the Earth and the asteroid's orbital plane (PlAng). The reduced images are shown in Figure 1, in which the direction to the Sun and the direction of the asteroid's orbital motion are indicated. The Earth crossed the orbital plane of the comet during the observational period, being just $+0\overset{\circ}{.}01$ above this plane during the observation of 2015 January 7. No dust features that could be associated with early activity, such as neck-line or trail, are seen. The Sloan r' magnitudes shown in Table 1 are computed on circular apertures of radius 2″. To set an upper limit to the asteroid's size, we converted the r' magnitudes to absolute magnitudes H_v by the relation

$$H_v = m_v - 5\log(R\Delta) + 2.5\log[\phi(\alpha)], \quad (1)$$

Table 1
Log of the Observations

UT YYYY/MM/DD HH:MM	Days to Perihelion	r' mag	R (AU)	Δ (AU)	α (deg)	PsAng (deg)	PlAng (deg)
2015 Dec 17 22:39	−91.8	21.64 ± 0.01	2.327	1.656	21.13	65.79	+1.00
2015 Dec 30 21:53	−78.9	22.06 ± 0.01	2.317	1.790	23.53	67.67	+0.37
2016 Jan 07 22:55	−70.8	22.28 ± 0.01	2.311	1.879	24.47	68.65	+0.01
2016 Jan 25 20:17	−52.9	22.41 ± 0.01	2.301	2.087	25.33	70.64	−0.66

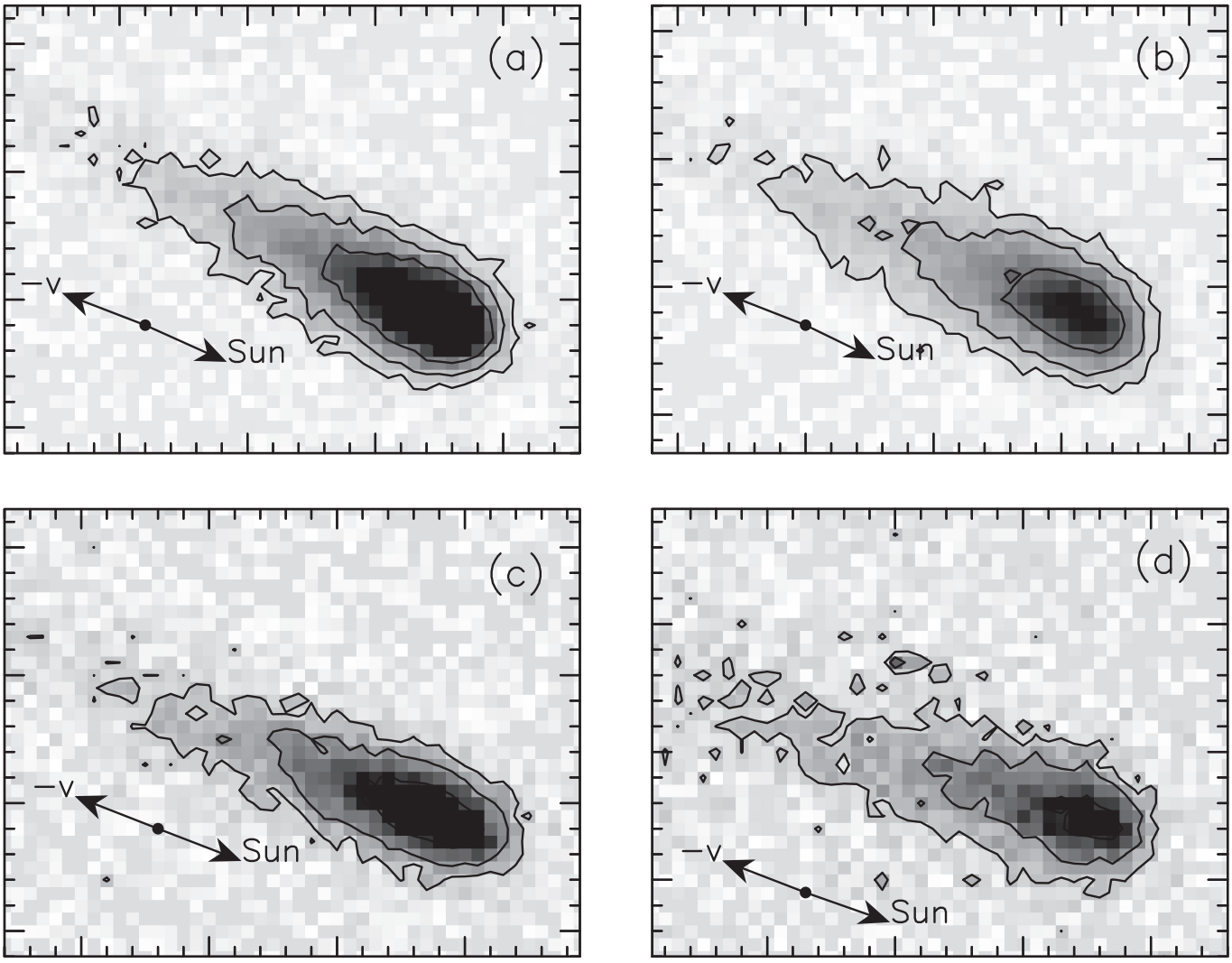

Figure 1. Median stack images of P/2015 X6 obtained with the OSIRIS instrument of the 10.4 m GTC through a Sloan r' filter, on UT 2015 December 7 (a), 2015 December 30 (b), 2016 January 7 (c), and 2016 January 25 (d). North is up, east to the left. The directions to the Sun and the negative of the orbital velocity motion are shown. The spatial dimensions of the images at the asteroid's distance (in km), in each panel, are as follows: (a) 13,728 × 10,677; (b) 14,839 × 11,541; (c) 15,577 × 12,115; (d) 17,301 × 13,456.

where m_v is the apparent visual magnitude and $\phi(\alpha)$ is the ratio of the scattered flux at phase angle α to that at $\alpha = 0°$. To obtain m_v from r' magnitudes we used the relationship of Fukugita et al. (1996):

$$m_v = r' - 0.49(B - V) + 0.11, \quad (2)$$

where we assumed the solar $B - V = +0.65$ (Cox 2000). Then, we obtained a maximum $H_v = +18.16$. We adopt the HG formulation (Bowell et al. 1989) with parameter $g = 0.15$ (appropriate for a C-type asteroid). From the a–i and a–e albedo maps of Masiero et al. (2011), a geometric albedo of $p_v \sim 0.1$ is obtained. However, all the objects found with sustained activity are from type C-complex (Licandro et al. 2011, 2013) and have darker albedos ($p_v \sim 0.05$). Then, adopting the formula of Harris & Lagerros (2002) relating geometric albedo to asteroid diameter D (in km),

$$D = \frac{1329}{\sqrt{p_v}} 10^{-0.2H_v}, \quad (3)$$

we obtain a diameter D in the range 980–1390 m for p_v between 0.05 and 0.1. This provides a very stringent upper limit for the asteroid's size, because the dust coma is likely dominating the observed brightness in the 2″ aperture, but would be a useful ingredient for the discussion of the dust models as described in Section 4.

3. THE MODEL

In order to perform a theoretical interpretation of the obtained images, and to retrieve the dust parameters, we used our Monte Carlo dust tail code, which has been used previously on several works on activated asteroids and comets, including comet 67P/Churyumov–Gerasimenko, the target of *Rosetta* (e.g., Moreno et al. 2016). The model computes the position on the sky plane, and the contributions to the tail brightness of a large number of particles ejected from the nucleus since a given epoch, under certain hypotheses about the physical properties of the particles and their size distribution, and the rate of dust mass loss. It is assumed that the particles, after leaving the object's surface, are subjected to the forces of solar radiation pressure and gravity. We neglect the object's gravity, an assumption valid for small objects. Under those conditions, the trajectory of the particles becomes Keplerian, being defined by their orbital elements, which are functions of their sizes and ejection velocities (e.g., Fulle 1989).

The ratio of radiation pressure to the gravitational force exerted on each particle is given by the β parameter, expressed as $\beta = C_{\rm pr} Q_{\rm pr}/(2\rho r)$, where $C_{\rm pr} = 1.19 \times 10^{-3}$ kg m^{-2}, $Q_{\rm pr}$ is the radiation pressure coefficient, and ρ is the particle density. $Q_{\rm pr}$ is taken as 1, because it converges to that value for absorbing particles of radius $r \gtrsim 1$ μm (see, e.g., Moreno et al. 2012c, their Figure 5).

A number of simplifying assumptions about the physical parameters of the dust must be made in order to make the problem tractable. Thus, the particle density is taken as 1000 kg m^{-3}, and the geometric albedo is set to $p_v = 0.04$, indicative of dark material of carbonaceous composition (see, e.g., Moreno et al. 2012c). In addition, a linear phase coefficient of 0.03 mag deg^{-1} was used to correct for the phase function of the dust particles, a typical value found for comet dust in the range $1° \leqslant \alpha \leqslant 30°$ (Meech & Jewitt 1987). The particles are assumed to be broadly distributed in size, with minimum and maximum particle radii set initially to 1 μm and 1 cm, and following a power-law function of index κ. In order to keep the fitting parameters to a minimum, we set this value to $\kappa = -3.3$, which is within the range of previous estimates of the size distribution of particles ejected from activated asteroids and comets. Isotropic ejection of the particles is assumed.

The ejection velocity of the particles will depend on the activation mechanism involved, which is unknown. In previous works on activated asteroids, we assumed ejection velocities depending on the particle size following a function of the kind $v \propto \beta^{\gamma}$. Values of γ of order 0.5, derived from simplified hydrodynamic considerations, have been used by many authors (including ourselves) for activity driven by ice sublimation. A weak correlation between velocity and mass (or size) has been obtained for fragments ejected in collision experiments (e.g., Giblin 1998), in the range 0–0.5, with a mean value of 0.23. We have, in fact, obtained values of γ as low as ~0.05 in the analysis of the tails of activated asteroid (596) Scheila, which was likely the result of an impact (Moreno et al. 2011b).

On the other hand, recent work on comet 67P, the target of *Rosetta*, has shown that the velocity of the particles, measured in situ from OSIRIS and GIADA instruments, does not show any evident trend regarding size when the comet was far from perihelion (3.6–3.4 AU) (Rotundi et al. 2015). Closer to the Sun (3.36–2.29 AU), the size dependence, estimated with the same instrumentation, became more apparent, being characterized by a steep power-law function, although with a considerable dispersion around the most probable value ($\gamma = 0.96 \pm 0.54$, Della Corte et al. 2015). Taking into account these results and the uncertainty in the particle ejection mechanism, we consider two different models by adopting two kinds of function for the ejection velocity: a customary power law given by $v = v_0 \beta^{\gamma}$, which will be called Model 1, and a random function of the form $v = v_1 + \zeta v_2$, where ζ is a random number in the interval [0, 1] and v_1 and v_2 are the fitting parameters. This model will be referred as to Model 2.

For the dust loss rate, we have adopted a half-Gaussian function whose maximum denotes the peak dust loss rate ($\dot{M}_0$), located at the start of the particle emission event (t_0). The half-width at half-maximum (HWHM) of the Gaussian is a measure of the effective time span of the event.

For Model 1, we have a set of five fitting parameters in total, $\dot{M}_0$, t_0, HWHM, v_0, and γ, and for Model 2, we also have five fitting parameters, namely $\dot{M}_0$, t_0, HWHM, v_1, and v_2. To fit the observed brightnesses of dust tails, we searched for a minimum of the function $\chi = \sum \sigma_i$, where the summation is extended to the four images under consideration, and $\sigma_i = \sqrt{(\sum [\log(I_{\rm obs}(i)) - \log(I_{\rm fit}(i))]^2 / N(i))}$, where $I_{\rm obs}(i)$ and $I_{\rm fit}(i)$ are the observed and modeled tail brightness, and $N(i)$ is the number of pixels in image i. In order to avoid regions of the images contaminated by field stars, the summation was restricted to pixels outside those regions. The minimization procedure was performed by the multidimensional downhill simplex algorithm (Nelder & Mead 1965), as described in Press et al. (1992). Since the algorithm always searches for a local minimum in the five-dimensional space of parameters, we used different starting simplexes in order to increase the probability that the minimum of the different minima found was the deepest one.

We performed a preliminary, zeroth-order analysis of the images by constructing a syndyne–synchrone map for each observing date. From those maps, we inferred that the activation time of the asteroid should be close in time to the discovery date, owing to the absence of dust features that could have shown up at the corresponding locations of synchrones approximately two months before discovery or earlier. In particular, no neck-line or trail features appear in the image from 2016 January 7 (PlAng ~ 0°), which could have indicated past activity. In addition, there are no dust condensations along the direction of isolated synchrones, which could have indicated short bursts of activity (e.g., the case of P/2012 F5 (Gibbs), Moreno et al. 2012a), or several separated short bursts, as in the case of P/2013 P5 (Jewitt et al. 2013; Moreno et al. 2014). According to this, it is reasonable to start the search for a minimum in the function χ defined above by placing the activation time (t_0) between a few days before the discovery date (102.5 days before perihelion) and about 60 days before. Regarding the duration of the activity, the smooth variation in absolute magnitudes (from $H_v = 17.88$ to $H_v = 18.16$, see Equation (1)) over the ~40 days period of observation and the aforementioned lack of single-synchrone dust features would

Table 2
Best-fit Parameters of the Models

	$\dot{M}_0$ (kg s^{-1})	t_0 (days)	HWHM (days)	v_0 (m s^{-1})	v_1 (m s^{-1})	v_2 (m s^{-1})	γ	Total mass (kg)	χ
Model 1	$1.0^{+0.3}_{-0.1}$	-120^{+10}_{-10}	$75^{+\infty}_{-25}$	$0.32^{+0.09}_{-0.08}$	…	…	$0.12^{+0.05}_{-0.07}$	4.6×10^6	0.122
Model 2	$1.6^{+0.5}_{-0.3}$	-128^{+30}_{-15}	$103^{+\infty}_{-20}$	…	$0.3^{+0.7}_{-0.3}$	$9.1^{+2.4}_{-4.0}$	…	8.8×10^6	0.120
Model 3	41.4	−131	2.0	…	0.08	1.0	…	6.0×10^6	0.159

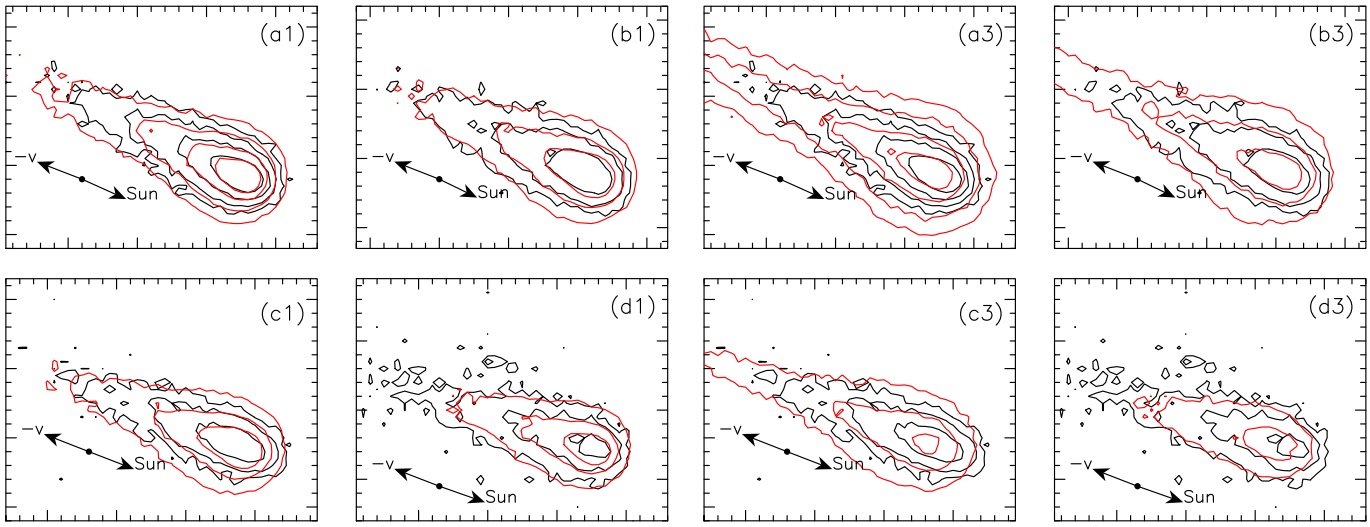

Figure 2. Measured (black) and modeled (red) isophotes for Model 1 (four leftmost panels (a1)–(d1)) and Model 3 (four rightmost panels (a3)–(d3)). The panels correspond to the same dates as in Figure 1. The innermost isophote levels are 1.5×10^{-14} solar disk intensity units, and decrease in factors of two outward.

suggest a long-lasting process and not an impulsive, short-duration event, such as a collision with another body. In any case, we considered both long- and short-duration events by varying HWHM in a wide range between a few days and several months in the starting simplex of the search of the five-dimensional parameter space. For the peak dust mass loss, we imposed a wide range between a minimum of 0.1 kg s^{-1} and 100 kg s^{-1}, while for the velocities we set broad limits for the parameters v_0, v_1, and v_2, so that the velocities ranged from 0 to 5×10^3 m s^{-1} (the mean velocity in the asteroid belt), and the parameter γ from 0.5 to 0, i.e., from typical gas drag to a nearly flat distribution of velocities.

4. RESULTS AND DISCUSSION

The resulting best-fit parameters for Models 1 and 2 are given in Table 2. We consider a limiting value of $\chi \leqslant 0.15$ to treat a fit as acceptable. The uncertainties provided correspond to the range of variation of the best-fit parameter for which $\chi \leqslant 0.15$. Models 1 and 2 show very similar χ values and very similar isophote fields, so we provide only the results of Model 1 in terms of those isophote fields (Figure 2, panels (a1)–(d1)). The peak dust loss rate varies between 1 kg s^{-1} and 1.6 kg s^{-1}, while similar activation times are found for both models: 120 and 128 days before perihelion for Models 1 and 2, respectively. The HWMH are also close between the two models: 75 days for Model 1 and 84 days for Model 2. The greatest difference between the models is found in the range of ejection velocities. For Model 1, the minimum velocity, corresponding to the largest particles ejected ($r = 1$ cm), is 1 m s^{-1}, and the maximum (for particles of radius 1 μm) is only a factor of three larger, because of the low value of $\gamma = 0.12$. However, for Model 2, we found a broader range between 0.29 and 9.8 m s^{-1}, giving a median value of ∼5 m s^{-1}. If the minimum velocities found were to correspond to escape velocities, then, for Model 1, we would obtain asteroid diameters between 1544 and 1890 m (for bulk densities of 3000 and 2000 kg m^{-3}, respectively), while for Model 2, the diameters would range from 450 to 550 m, for the same densities. According to the upper limit on asteroid size imposed by the determination of absolute magnitude (D in the range 980–1390m, see above), Model 1 would not meet this constraint, and consequently should be rejected. However, there is not a priori a specific physical reason to think that the slowest particles should be ejected at velocities near the escape velocity, because this would depend on the ejection mechanism involved, which is not known.

Let us assume first a rotational instability as the cause of the event. A short-duration event was needed to explain the activity in P/2012 F5 (Gibbs) (e.g., Moreno et al. 2012a; Stevenson et al. 2012), and, although an impact with another object was invoked as the cause, the discovery of several trailing fragments in follow-up images by Drahus et al. (2015) led them to infer a rotational instability as the most likely mechanism. For P/2012 F5, we inferred quite low dust ejection velocities, of the order of 8–10 cm s^{-1} (Moreno et al. 2012a). This would, in fact, be compatible with rotational instability causing particles to be ejected at velocities near the escape velocity of the parent body. In the case of asteroid P/2013 R3, which was observed to break apart into several fragments, a rotationally induced mechanism was also invoked, and the inferred dust speed was also low, of the order of 1 m s^{-1} (Jewitt et al. 2014). In contrast to P/2012 F5, however, the activity was sustained for a period of 2–3 months, the

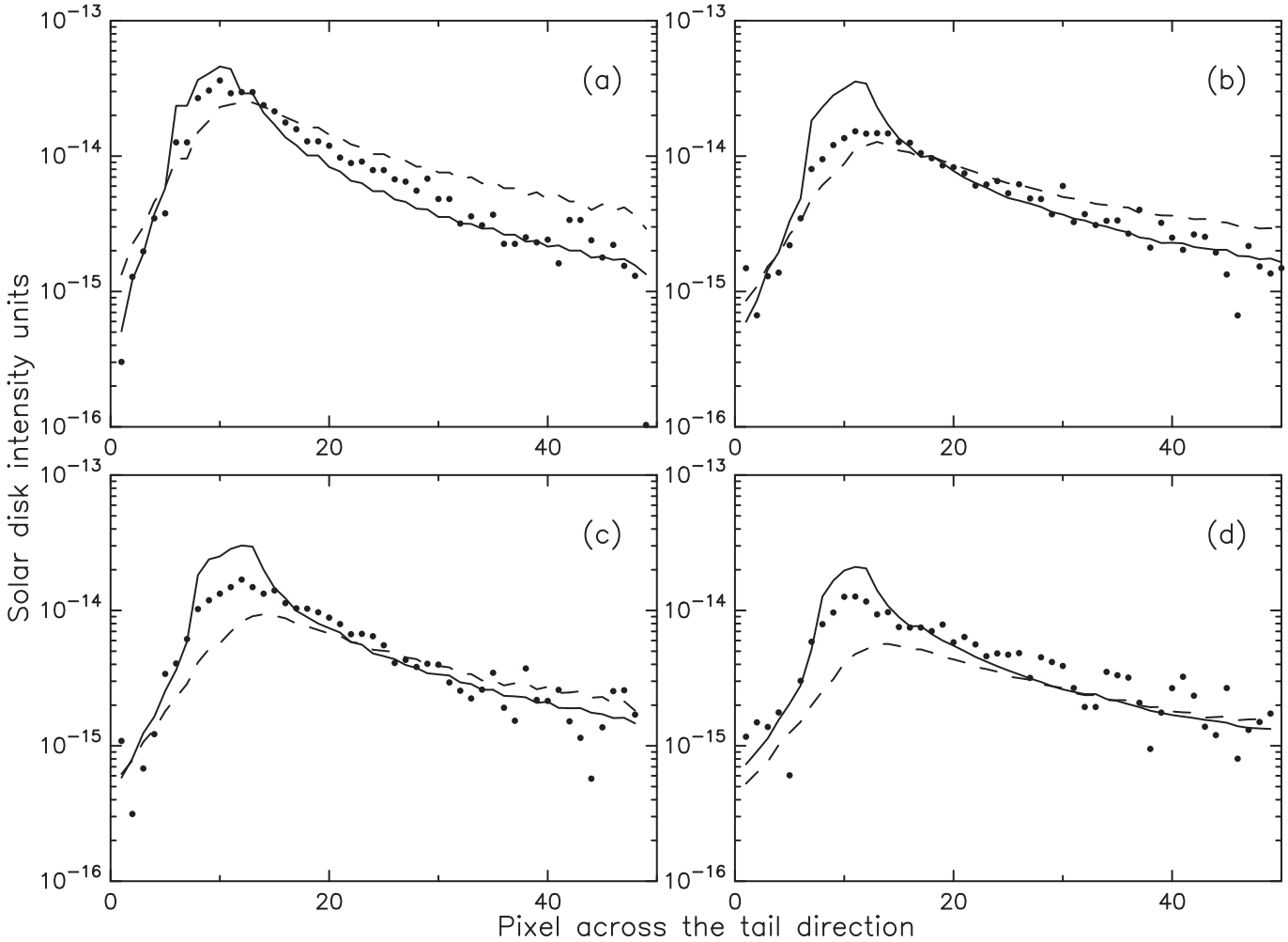

Figure 3. Scans along the direction of the tail for the observed images (solid circles), Model 1 images (solid lines), and Model 3 images (dashed lines). Labels (a)–(d) correspond to the different observing dates as shown in Figure 1.

fragments becoming individual dust sources (Jewitt et al. 2014). In the case of P/2015 X6, we have also inferred sustained activity, of the order of months, and low velocities (2–5 m s^{-1} on average, depending on the model), so that in principle its activation mechanism would be compatible with a rotational instability. It is important to note, however, that we have not seen any fragments, although this is hampered by the spatial resolution and the limiting magnitude reachable with the instrumentation used.

Another possibility is the occurrence of an impact that excavated surface layers of the asteroid, exposing ices that might exist in its interior to sunlight, or, alternatively, that on some surface regions of the asteroid the temperature becomes high enough when the asteroid approaches perihelion that surface ices can sublimate. Any of those cases would lead to sustained dust activity induced by the sublimation, as is very likely the case for activated asteroids 133P, 238P, 313P, and 324P (Hsieh et al. 2004, 2011; Hsieh & Sheppard 2015; Jewitt et al. 2015; Pozuelos et al. 2015), although the strongest reason for this mechanism to occur is the fact that they show recurrent activity when near perihelion. In consequence, ice sublimation would very well explain the sustained activity we have found for this object, but more observations during future perihelion passages would be needed to assess the likelihood of this mechanism.

We could not find a solution with a comparable fit quality to the best-fit Models 1 or 2 for an impulsive, short-duration event. Thus, limiting the HWHM to 2 days or less for the parameters of Model 1, the code converges to a solution with a very large $\chi = 0.435$. On assuming the parameters of Model 2, the results improve significantly, but still $\chi = 0.159$, far from the best χ values of Models 1 and 2. The isophote fields from this short-burst model (called Model 3) are shown in Figure 2, together with the results of Model 1, and the best-fit parameters are shown in Table 2. Figure 3 displays intensity scans along the tails of the best-fit Models 1 and 3, in which one can see the much better agreement of Model 1 with the data as compared with Model 3. In summary, a short-duration event seems unlikely.

5. CONCLUSIONS

The following conclusions can be drawn from the GTC observations and the dust tail modeling of the activated asteroid P/2015 X6.

1. The analysis performed by a simultaneous multidimensional fit to the four available images of the dust tail implies most likely a pattern of sustained activity spanning at least two months until the most recent observation, but probably much longer. The nature of the

activation could not be determined, because both ice sublimation and rotational instability can be invoked as plausible mechanisms. Future near-perihelion observations would be needed to search for recurrent activity. The possibility of a short-duration burst of activity that could be caused by an impact and subsequent ejection of material is unlikely from the model fits.

2. Two models of ejection velocity, one based on a customary $v \propto \beta^{\gamma}$ (Model 1) and another based on a random distribution of the kind $v = v_1 + \zeta v_2$ (where ζ is a random number in the interval (0, 1)) (Model 2), have been proposed. For Model 1, a nearly flat distribution of particle velocities is found, in the range 1–3 m s^{-1}. The best fits for Model 2 imply a wider range of velocities, 0.3–10 m s^{-1}. The quality of the fits obtained was very similar, so neither of those models can be favored over the other.
3. The derived rate of dust mass loss is characterized by peak values of 1 and 1.6 kg s^{-1}, with time spans of ~75 and ~100 days, for Models 1 and 2, respectively. The total dust mass ejected from the activation date until the most recent observation reported was 5–9 $\times$ 10^6 kg.
4. The activation times found were 18 and 26 days before the discovery date for Models 1 and 2, respectively. No dust features that could be attributed to older activity were found.

This article is based on observations made with the Gran Telescopio Canarias, installed in the Spanish Observatorio del Roque de los Muchachos of the Instituto de Astrofísica de Canarias, in the island of La Palma.

This work was supported by contract AYA2015-67152-R from the Spanish Ministerio de Economía y Competitividad. J. Licandro gratefully acknowledges support from contract ESP2013-47816-C4-2-P.

REFERENCES

Bowell, E., Hapke, B., Domingue, D., et al. 1989, in Asteroids II, ed. R. P. Binzel, T. Gehrels, & M. S. Matthews (Tucson, AZ: Univ. Arizona Press), 524
Cepa, J. 2010, Highlights of Spanish Astrophysics V (Berlin: Springer)
Cepa, J., Aguiar, M., Escalera, V., et al. 2000, Proc. SPIE, 4008, 623
Cox, A. N. 2000, Allen's Astrophysical Quantities (4th ed.; Berlin: Springer)
Della Corte, V., Rotundi, A., Fulle, M., et al. 2015, A&A, 583, 13
Drahus, M., Waniak, W., Tendulkar, S., et al. 2015, ApJL, 802, L8
Finson, M., & Probstein, R. 1968, ApJ, 154, 327
Fukugita, M., Ichikawa, T., Gunn, J. E., et al. 1996, AJ, 111, 1748
Fulle, M. 1989, A&A, 217, 283
Fulle, M., Colangeli, L., Agarwal, J., et al. 2010, A&A, 522, 63
Gibbs, A. R., Sato, H., Ryan, W. H., et al. 2012, CBET, 3069, 1
Giblin, I. 1998, P&SS, 46, 921
Haghighipour, N. 2009, M&PS, 44, 1863
Harris, A. W., & Lagerros, J. S. V. 2002, Asteroids III (Tucson, AZ: Univ. Arizona Press)
Hsieh, H. H., & Jewitt, D. 2006, Sci, 312, 561
Hsieh, H. H., Jewitt, D., & Fernández, Y. 2004, AJ, 127, 2997
Hsieh, H. H., Jewitt, D., & Ishiguro, M. 2009, AJ, 137, 157
Hsieh, H. H., Jewitt, D., Lacerda, P., et al. 2010, MNRAS, 403, 363
Hsieh, H. H., Kaluna, H. M., Novaković, B., et al. 2013, ApJL, 771, L1
Hsieh, H. H., Meech, K., & Pittichova, J. 2011, ApJL, 736, L18
Hsieh, H. H., & Sheppard, S. S. 2015, MNRAS, 454, L81
Hsieh, H. H., Yang, B., & Haghighipour, N. 2012, ApJ, 744, 9
Jewitt, D. 2012, AJ, 143, 21
Jewitt, D., Agarwal, J., & Hsieh, H. 2015, Asteroids IV (Tucson, AZ: Univ. Arizona Press)
Jewitt, D., Agarwal, J., Li, J., et al. 2014, ApJL, 784, L8
Jewitt, D., Agarwal, J., Weaver, H., et al. 2013, ApJL, 778, L21
Jewitt, D., Weaver, H., Mutchler, M., et al. 2011, ApJL, 733, L4
Jewitt, D., Yang, B., & Haghighipour, N. 2009, AJ, 137, 4313
Kresak, L. 1982, BAICz, 33, 104
Licandro, J., Campins, H., Tozzi, G. P., et al. 2011, A&A, 532A, 65L
Licandro, J., Moreno, F., & de León, J. 2013, A&A, 550A, 17L
Lilly, E., & Weryk, R. 2015, CBET, 4221
Masiero, J. R., Mainzer, A. K., Grav, T., et al. 2011, ApJ, 741, 68
Meech, K. J., & Jewitt, D. C. 1987, A&A, 187, 585
Moreno, F., Lara, L. M., Licandro, J., et al. 2011a, ApJL, 738, L16
Moreno, F., Licandro, J., Álvarez-Iglesias, C., et al. 2014, ApJ, 781, 118
Moreno, F., Licandro, J., & Cabrera-Lavers, A. 2012a, ApJL, 761, L12
Moreno, F., Licandro, J., Ortiz, J. L., et al. 2011b, ApJ, 738, 130
Moreno, F., Pozuelos, F., Aceituno, F., et al. 2012b, ApJ, 752, 136
Moreno, F., Pozuelos, F., Aceituno, F., et al. 2012c, ApJ, 752, 136
Moreno, F., Snodgrass, C., Hainaut, O., et al. 2016, A&A, 587, A155
Nelder, J. A., & Mead, R. 1965, CompJ, 7, 308
Pozuelos, F. J., Cabrera-Lavers, A., Licandro, J., et al. 2015, ApJ, 806, 102
Press, W. H., Teukolsky, S. A., Vetterling, W. T., & Flannery, B. P. 1992, Numerical Recipes in FORTRAN (Cambridge: Cambridge Univ. Press)
Rotundi, A., Sierks, H., Della Corte, V., et al. 2015, Sci, 347, 3905
Stevenson, R., Kramer, E. A., Bauer, J. M., et al. 2012, ApJ, 759, 142
Tubbiolo, A. F., Bressi, T. H., Wainscoat, R. J., et al. 2015, MPEC, 2015-X180